The Astrophysical Journal, 725:605–614, 2010 December 10 doi:10.1088/0004-637X/725/1/605

POLYCYCLIC AROMATIC HYDROCARBON AND EMISSION LINE RATIOS IN ACTIVE GALACTIC NUCLEI AND STARBURST GALAXIES

Dinalva A. Sales[1], M. G. Pastoriza[1,2], and R. Riffel[1]
[1] Departamento de Astronomia, Universidade Federal do Rio Grande do Sul. Av. Bento Gonçalves 9500, Porto Alegre, RS, Brazil;
dinalva.aires@ufrgs.br, pastoriza@ufrgs.br, riffel@ufrgs.br
[2] Conselho Nacional de Desenvolvimento Científico e Tecnológico, Brazil
Received 2010 March 15; accepted 2010 October 1; published 2010 November 19

ABSTRACT

We study the polycyclic aromatic hydrocarbon (PAH) bands, ionic emission lines, and mid-infrared continuum properties in a sample of 171 emission line galaxies taken from the literature plus 15 new active galactic nucleus (AGN) *Spitzer* spectra. We normalize the spectra at $\lambda = 23\,\mu$m and grouped them according to the type of nuclear activity. The continuum shape steeply rises for longer wavelengths and can be fitted with a warm blackbody distribution of $T \sim 150$–300 K. The brightest PAH spectral bands (6.2, 7.7, 8.6, 11.3, and 12.7 μm) and the forbidden emission lines of [Si II] 34.8 μm, [Ar II] 6.9 μm, [S III] 18.7 and 33.4 μm were detected in all the starbursts and in ∼80% of the Seyfert 2. Taking under consideration only the PAH bands at 7.7 μm, 11.3 μm, and 12.7 μm, we find that they are present in ∼80% of the Seyfert 1, while only half of this type of activity show the 6.2 μm and 8.6 μm PAH bands. The observed intensity ratios for neutral and ionized PAHs (6.2 μm/7.7 μm × 11.3 μm/7.7 μm) were compared to theoretical intensity ratios, showing that AGNs have higher ionization fraction and larger PAH molecules (⩾180 carbon atoms) than SB galaxies. The ratio between the ionized (7.7 μm) and the neutral PAH bands (8.6 μm and 11.3 μm) are distributed over different ranges for AGNs and SB galaxies, suggesting that these ratios could depend on the ionization fraction, as well as on the hardness of the radiation field. The ratio between the 7.7 μm and 11.3 μm bands is nearly constant with the increase of [Ne III]15.5 μm/[Ne II] 12.8 μm, indicating that the fraction of ionized to neutral PAH bands does not depend on the hardness of the radiation field. The equivalent width of both PAH features show the same dependence (strongly decreasing) with [Ne III]/[Ne II], suggesting that the PAH molecules, emitting either ionized (7.7 μm) or neutral (11.3 μm) bands, may be destroyed with the increase of the hardness of the radiation field.

Key words: galaxies: Seyfert – galaxies: starburst – infrared: ISM – ISM: molecules – techniques: spectroscopic

Online-only material: color figures

1. INTRODUCTION

The mid-infrared (mid-IR) spectra of galaxies either with an active nucleus (AGN) and/or a starburst (SB) show emission features attributed to polycyclic aromatic hydrocarbons (PAHs), which can be considered to originate in very small amorphous carbon dust grains or very large carbon-rich ring molecules (e.g., Puget & Leger 1989; Draine & Lee 1984; Draine & Li 2001). The most prominent, well-known PAH emissions are the 6.2 μm, 7.7 μm, 8.6 μm, 11.2 μm, and 12.7 μm bands (e.g., Roche et al. 1991; Genzel et al. 1998; Weedman et al. 2005; Buchanan et al. 2006). Besides, the mid-IR spectral region also presents prominent forbidden ionic emission lines, such as [Ne II]12.8 μm, [Ne V]14.3 μm, [Ne III]15.5 μm, [S III]18.7 μm and 33.48 μm, [O IV]25.89 μm and [Si II]34.8 μm (e.g., Sturm et al. 2002; Bernard-Salas et al. 2009).

The nature of the ionizing source can be assessed by computing the intensity ratios between forbidden lines such as [Ne II]12.8 μm, [Ne III]15.5 μm, and [Ne V]14.3 μm (e.g., Voit 1992a). In addition, the detection of [Ne V] at 14.3 μm and 24.2 μm or of [Ne VI] at 7.6 μm, due to ions of high ionization potential, is evidence of a hard radiation field associated with an AGN (Genzel et al. 1998; Sturm et al. 2000).

Several diagnostic diagrams based on the line intensity ratios between the brightest ionic lines and the PAH features have been proposed to classify the mid-IR spectra of galaxies according to the degree of activity (AGNs, low-ionization nuclear emission-line regions (LINERs), and SB galaxies). For instance, Genzel et al. (1998), using data from the Short Wavelength Spectrometer (SWS) on board the *Infrared Space Observatory*, propose the diagnostic diagram, [O IV]25.9 μm/[Ne II]12.8 μm versus the strength of the 7.7 μm PAH band, to separate star-forming galaxies from AGNs.

From a study of the mid-IR spectra of quiescent spirals, Galactic H II regions, planetary nebulae, and photodissociation regions (PDRs), Galliano (2006) found that the ratios between the 6.2 μm/8.6 μm and 7.7 μm/8.6 μm PAH bands do not vary significantly, while the ratios 6.2 μm/11.3 μm and 7.7 μm/11.3 μm vary over one order of magnitude. They concluded that the properties of the PAHs for different types of galaxies are very similar and that variations of the PAH band ratios are due to the fraction of ionized to neutral PAH molecules. Thus, this ratio could be used to analyze the physical conditions of the molecular gas in the regions where the emission originated. In addition, Gordon et al. (2008) found that the equivalent width (EW) of PAH features, observed in H II regions of the M101 galaxy, is correlated with the ionization index and does not depend on the H II region metallicity.

According to Smith et al. (2007), the ionized to neutral fraction of PAHs can be estimated using the PAH 7.7 μm/11.3 μm ratio, which is sensitive to the type of nuclear activity, decreasing from SB to Seyfert. These authors suggest that this behavior is due to the selective destruction of the 7.7 μm PAH molecule with the increasing hardness of the radiation field (similar results are found by O'Dowd et al. 2009, Hunt et al. 2010, and Kaneda et al. 2008). Such results are supported

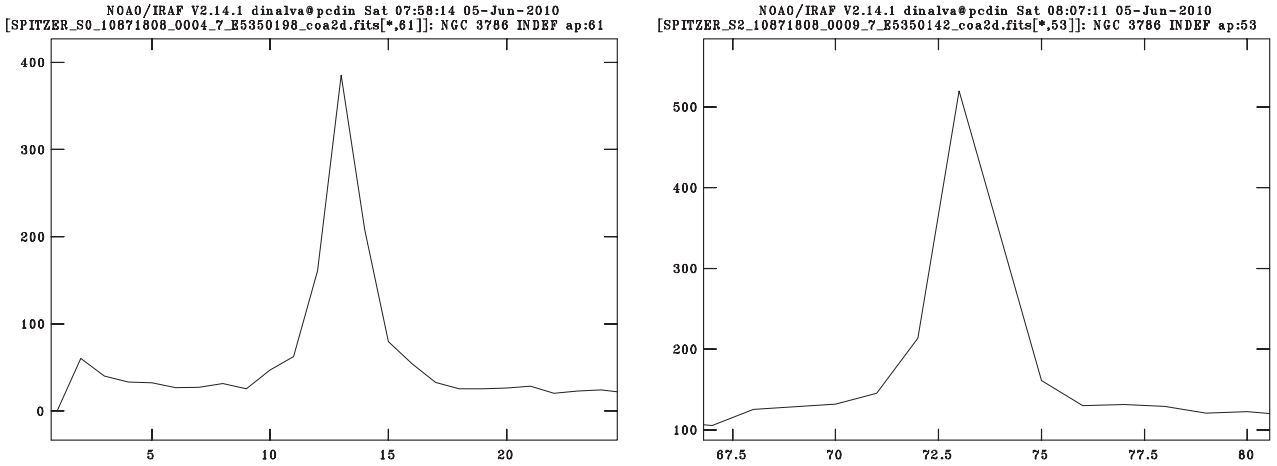

Figure 1. Spatial emission profile of NGC 3786 for the SL (left) and LL (right) modules.

by laboratory experiments, which show that certain PAHs are effectively destroyed by individual UV and X-ray photons, and cannot survive within a few kiloparsecs from an active nucleus, unless they are shielded from the AGN's X-ray emission by absorbing material (Voit 1992b).

It is worth mentioning that the above results, concerning the ionization fraction of PAH bands in AGNs, are carried out with small samples of this type of object. Therefore, we use the largest sample of AGNs and SB galaxies available to date in the *Spitzer* public archive to study in detail the effect of the hardness of the radiation field on the PAH band emission in these kinds of galaxies. This paper is structured as follows: in Section 2 we describe the sample selection, data reduction process, and emission line measurements. In Section 3, we present results and a discussion on the shape of the continuum spectra, emission line frequency, and diagnostic diagrams of PAH band ratios and emission lines ratios. In Section 4, we discuss the behavior of the ionization fraction and EW of PAH bands with the hardness of the radiation field. A summary and conclusion are presented in Section 5.

2. THE SAMPLE

We have analyzed a well-defined sample of 186 galaxies which have *Spitzer* spectra available from the public archive: 83 AGNs taken from Gallimore et al. (2010), 22 SBs from Brandl et al. (2006), 59 H II and LINERs from Smith et al. (2007) and 7 H II regions of M101 galaxy from Gordon et al. (2008), plus 15 AGN *Spitzer* spectra published here for the first time. Details on the reduction process of the 15 new objects are given below.

2.1. Data Reduction

The 15 new spectra of AGN galaxies (4 Sy 1 and 11 Sy 2) were obtained from the *Spitzer* public archive. Observations were performed with the Infrared Spectrograph (IRS; Houck et al. 2004) using the short–low (SL) and long–low (LL) modules, covering the interval between 5 μm and 36 μm with a resolving power of 64–128. The raw data were processed using the *Spitzer* PIPELINE version 17.2.[3] The nuclear spectra were extracted using the *Spitzer* IRS Custom Extractor—SPICE.[4] Default point-source extractions were selected for all objects. Only a few sources show a noticeable step in flux between the overlapping LL and LS module spectra, which results from the extended circumnuclear emission contribution to the size SL module slit of $3\farcs7 \times 57''$ and LL module slit of $10\farcs7 \times 168''$. Although the observed regions of almost all of the galaxies are large in both modules, the AGN light dominates the spectra. Figure 1 shows the emission spatial profile of NGC 3786. Note that the luminosity falls off to almost zero for ≈3 pixels from the center of the nucleus. For this galaxy, 3 pixels correspond to ≈1 kpc, adopting a radial velocity of 2678 km s^{-1} and a Hubble constant of 74 km s^{-1} Mpc^{-1}.

Table 1
Sample Properties

Name	R.A.[a]	Decl.[a]	z[a]
	Sey 1		
Mrk 279	$13^h53^m03\overset{s}{.}4$	$+69^h18^m30^s$	0.030451
Mrk 334	$00^h03^m09\overset{s}{.}6$	$+21^h57^m37^s$	0.021945
Mrk 478	$14^h42^m07\overset{s}{.}4$	$+35^h26^m23^s$	0.079055
NGC 4748	$12^h52^m12\overset{s}{.}4$	$-13^h24^m53^s$	0.014630
	Sey 2		
Mrk 3	$06^h15^m36\overset{s}{.}3$	$+71^h02^m15^s$	0.013509
Mrk 471	$14^h22^m55\overset{s}{.}4$	$+32^h51^m03^s$	0.034234
Mrk 609	$03^h25^m25\overset{s}{.}3$	$-06^h08^m38^s$	0.034488
Mrk 622	$08^h07^m41\overset{s}{.}0$	$+39^h00^m15^s$	0.023229
Mrk 883	$16^h29^m52\overset{s}{.}9$	$+24^h26^m38^s$	0.037496
Mrk 1066	$02^h59^m58\overset{s}{.}6$	$+36^h49^m14^s$	0.012025
NGC 1275	$03^h19^m48\overset{s}{.}1$	$+41^h30^m42^s$	0.017559
NGC 2622	$08^h38^m10\overset{s}{.}9$	$+24^h53^m43^s$	0.028624
NGC 3786	$11^h39^m42\overset{s}{.}5$	$+31^h54^m33^s$	0.008933
NGC 5728	$14^h42^m23\overset{s}{.}9$	$-17^h15^m11^s$	0.009353
NGC 7682	$23^h29^m03\overset{s}{.}9$	$+03^h32^m00^s$	0.017140

Note. [a] Taken from the NASA Extragalactic Database (NED).

The general parameters for the objects listed in Table 1 were taken from the NASA/IPAC Extragalactic Database (NED). All the spectra were corrected for redshift. The rest-frame spectra were grouped according to their activity and are shown in Figure 2.

2.2. Emission Line Measurements

For the 15 new AGNs listed in Table 1 and SBs taken from Brandl et al. (2006), low-resolution IRS spectra have been decomposed using the PAHFIT[5] code, described in detail by

[3] Available at: http://ssc.spitzer.caltech.edu/spitzerdataarchives/.
[4] Available at: http://ssc.spitzer.caltech.edu/postbcd/spice.html.
[5] Source code and documentation for PAHFIT are available at http://tir.astro.utoledo.edu/jdsmith/research/pahfit.php.

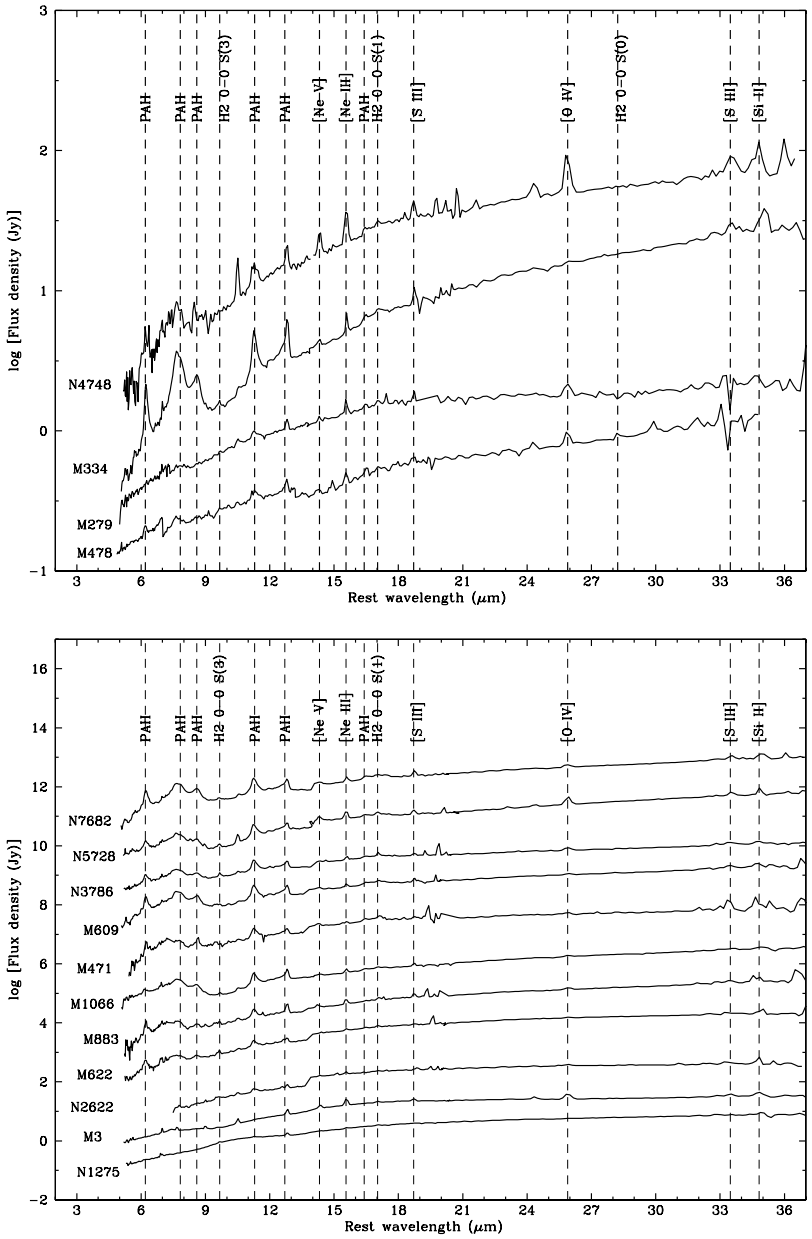

Figure 2. Calibrated spectra of the Sy 1 (top) and Sy 2 (bottom) galaxies. All spectra were ordered according to their shapes from a steeper spectrum (top) to a flatter one (bottom). Some emission lines are identified. All spectra were normalized at 23 μm.

Smith et al. (2007). In short, they assume that the IRS spectra are composed of dust continuum, starlight, prominent emission lines, and individual and blended PAH emission bands, and that the light is attenuated by extinction due to silicate grains.

The default input parameters of PAHFIT are (1) the infrared emission from a blackbody with $T = 5000$ K; (2) different weights for thermal dust continuum components represented by the temperatures 35, 40, 50, 90, 135, 200, 300 K; (3) spectral line features, including the pure rotational lines of the molecular hydrogen; and (4) dust features are represented by individual and blended Drude profiles, which are theoretical frequency profiles for a classical damped harmonic oscillator and are the best choice to model PAH emission. For more details see Smith et al. (2007).

With the above constraints we were able to isolate the PAH features and measure their fluxes, as well as those of the ionized gas emission lines. The fluxes and the EW are listed in Tables 2 and 3. We checked the consistency of the results with the LINER code (Pogge & Owen 1993) that integrates the flux of a Gaussian function fitted to the line, obtaining similar results in both procedures. The observed IRS spectra of Mrk 334, a Sy 1 galaxy, is shown in Figure 3, where we also plot the detailed components of the PAHFIT spectral decomposition model. Clearly, the model reproduces well the observed spectrum.

3. RESULTS AND DISCUSSION

3.1. New Spectra

The main goal of this section is to characterize the continuum shapes and spectral features observed in the 15 new objects listed in Table 1, with respect to the type of nuclear activity (Sy 1 and Sy 2). Therefore, we normalize to unity the continuum of all spectra at $\lambda = 23\,\mu$m and grouped them according to nuclear activity. For each AGN class, data were sorted according to spectral shape, from bluest to reddest, top to bottom of Figure 2, respectively. One can clearly see that the majority of spectra

Table 2
Aromatic Emission Line Strengths (10^{-16} W m^{-2}) and Equivalent Widths (μm)

Name	6.2 μm	EW	6.7 μm	EW	7.7 μm	EW	8.3 μm	EW	8.6 μm	EW	10.7 μm	EW	11.3 μm	EW	12.0 μm	EW	12.7 μm	EW	17.0 μm	EW
Sy 1																				
Mrk 279	2.88 ± 0.33	0.035	7.19 ± 0.81	0.095	15.6 ± 1.82	0.220	...	...	0.09 ± 0.26	0.001	0.84 ± 0.12	0.013	2.94 ± 0.36	0.049	...	...	0.15 ± 0.10	0.002	6.62 ± 0.89	0.154
Mrk 334	28.5 ± 0.30	0.548	9.92 ± 0.67	0.183	107 ± 2.88	1.881	7.98 ± 0.34	0.138	20.2 ± 0.24	0.351	1.12 ± 0.09	0.019	28.3 ± 0.35	0.479	8.05 ± 0.19	0.131	16.7 ± 0.39	0.263	18.5 ± 0.83	0.229
Sy 2																				
Mrk 3	0.77 ± 0.31	0.006	4.56 ± 0.63	0.037	38.2 ± 2.98	0.315	...	...	1.14 ± 0.35	0.009	1.22 ± 0.17	0.009	3.28 ± 0.55	0.022	1.61 ± 0.37	0.009	1.45 ± 0.16	0.008	39.2 ± 1.57	0.143
Mrk 471	2.67 ± 0.12	0.820	3.98 ± 0.32	1.030	6.78 ± 1.15	1.415	...	...	2.15 ± 0.09	0.382	0.05 ± 0.04	0.007	3.30 ± 0.22	0.474	0.56 ± 0.19	0.078	1.67 ± 0.29	0.226	5.18 ± 0.26	0.359
Mrk 609	16.9 ± 0.22	1.020	8.57 ± 0.49	0.485	58.0 ± 1.74	3.115	4.62 ± 0.20	0.245	11.7 ± 0.16	0.617	0.53 ± 0.07	0.027	17.7 ± 0.32	0.903	5.76 ± 0.23	0.282	10.4 ± 0.48	0.474	16.5 ± 0.66	0.469
Mrk 622	5.01 ± 0.19	0.516	2.26 ± 0.42	0.194	14.6 ± 1.65	0.986	...	...	1.71 ± 0.14	0.093	0.37 ± 0.07	0.015	6.45 ± 0.28	0.253	2.40 ± 0.18	0.089	4.41 ± 0.41	0.154	2.65 ± 0.49	0.044
Mrk 883	4.62 ± 0.14	1.100	4.68 ± 0.35	0.920	10.7 ± 1.18	1.630	...	...	1.33 ± 0.10	0.161	0.01 ± 0.04	0.001	3.76 ± 0.22	0.324	0.83 ± 0.18	0.068	1.37 ± 0.34	0.107	2.53 ± 0.30	0.111
Mrk 1066	47.0 ± 0.28	0.757	15.5 ± 0.58	0.263	199 ± 2.76	3.567	18.6 ± 0.37	0.340	31.9 ± 0.26	0.592	1.29 ± 0.11	0.020	52.1 ± 0.43	0.713	15.3 ± 0.23	0.181	30.9 ± 0.45	0.328	43.0 ± 1.41	0.325
NGC 1275	10.8 ± 0.25	0.097	18 ± 0.48	0.139	...	...	...	...	...	...	10.6 ± 0.10	0.043	17.4 ± 0.33	0.070	2.90 ± 0.22	0.011	...	...	53.9 ± 0.98	0.199
NGC 2622	2.75 ± 0.14	0.233	4.33 ± 0.37	0.339	...	...	...	...	...	...	0.32 ± 0.05	0.015	2.97 ± 0.21	0.135	0.78 ± 0.14	0.034	2.03 ± 0.13	0.086	2.42 ± 0.46	0.0472
NGC 5728	10.6 ± 0.32	0.379	4.11 ± 0.64	0.167	65.1 ± 3.00	3.050	4.88 ± 0.37	0.245	8.09 ± 0.31	0.424	0.04 ± 0.21	0.001	21.4 ± 0.65	0.783	3.97 ± 0.35	0.117	9.89 ± 0.78	0.258	32.6 ± 1.14	0.471
NGC 7682	40.4 ± 0.16	1.840	11.5 ± 0.35	0.456	160 ± 1.48	5.200	11.3 ± 0.16	0.328	29.7 ± 0.12	0.828	1.07 ± 0.05	0.024	40.9 ± 0.19	0.913	10.1 ± 0.12	0.221	24.0 ± 0.26	0.522	39.8 ± 0.55	0.641

Table 3
Atomic Emission Line Strengths (10^{-16} W m^{-2}) and Equivalent Widths (μm)

Name	[Ar II]6.9 μm	EW	[Ar III]8.9 μm	EW	[S IV]10.5 μm	EW	[Ne II]12.8 μm	EW	[Ne III]15.5 μm	EW	[S III]18.7 μm	EW	[O IV]25.9 μm	EW	[Fe II]25.9 μm	EW	[S III]33.4 μm	EW	[Si II]34.8 μm	EW
Sy 1																				
Mrk 279	0.70 ± 0.16	0.014	0.05 ± 0.10	0.001	0.60 ± 0.05	0.014	0.82 ± 0.05	0.022	1.26 ± 0.07	0.039	0.64 ± 0.10	0.024	1.10 ± 0.05	0.067	...	...	...	...	0.87 ± 0.13	0.088
Mrk 334	1.36 ± 0.09	0.036	0.06 ± 0.05	0.001	0.63 ± 0.03	0.016	5.32 ± 0.03	0.122	2.58 ± 0.04	0.050	2.91 ± 0.06	0.050	...	...	0.49 ± 0.06	0.008	3.82 ± 0.14	0.068	7.07 ± 0.14	0.129
Mrk 478	0.47 ± 0.03	0.012	0.06 ± 0.06	0.002	0.38 ± 0.04	0.016	0.59 ± 0.04	0.032	0.52 ± 0.01	0.032	0.40 ± 0.01	0.027	0.75 ± 0.02	0.066	...	...	... ± −	...	0.01 ± 0.06	0.001
NGC 4748	0.45 ± 0.21	0.030	0.28 ± 0.12	0.018	2.34 ± 0.09	0.144	1.14 ± 0.06	0.065	3.78 ± 0.12	0.123	1.83 ± 0.15	0.058	6.81 ± 0.13	0.269	...	...	2.69 ± 0.24	0.131	3.42 ± 0.29	0.167
Sy 2																				
Mrk 3	3.31 ± 0.19	0.040	2.63 ± 0.12	0.034	6.26 ± 0.08	0.072	8.75 ± 0.08	0.073	20.9 ± 0.12	0.111	6.70 ± 0.11	0.037	18.2 ± 0.10	0.159	...	...	4.25 ± 0.20	0.054	11.7 ± 0.20	0.156
Mrk 471	0.43 ± 0.06	0.153	...	...	0.12 ± 0.01	0.028	0.32 ± 0.02	0.064	0.19 ± 0.01	0.020	0.13 ± 0.02	0.013	0.36 ± 0.02	0.049	...	...	1.74 ± 0.03	0.285	2.03 ± 0.08	0.331
Mrk 609	1.02 ± 0.08	0.083	...	...	0.29 ± 0.02	0.022	2.22 ± 0.03	0.144	1.11 ± 0.04	0.047	1.19 ± 0.05	0.048	0.82 ± 0.03	0.034	...	...	1.59 ± 0.08	0.070	3.63 ± 0.13	0.159
Mrk 622	0.40 ± 0.08	0.046	...	...	0.34 ± 0.02	0.021	0.70 ± 0.03	0.036	0.73 ± 0.03	0.019	0.39 ± 0.07	0.009	0.73 ± 0.04	0.020	...	...	0.80 ± 0.09	0.028	3.51 ± 0.14	0.128
Mrk 883	0.55 ± 0.06	0.147	0.11 ± 0.02	0.019	0.26 ± 0.02	0.036	1.31 ± 0.02	0.150	0.96 ± 0.03	0.069	0.71 ± 0.03	0.043	0.91 ± 0.02	0.058	...	...	0.82 ± 0.05	0.052	2.58 ± 0.09	0.161
Mrk 1066	3.75 ± 0.12	0.096	0.83 ± 0.07	0.023	1.61 ± 0.04	0.038	9.60 ± 0.03	0.146	4.67 ± 0.09	0.055	4.80 ± 0.12	0.050	3.51 ± 0.22	0.031	0.25± 0.29	0.002	3.72 ± 0.22	0.035	11.2 ± 0.23	0.108
NGC 1275	1.89 ± 0.11	0.019	...	...	2.78 ± 0.05	0.017	3.37 ± 0.05	0.019	4.25 ± 0.14	0.023	1.77 ± 0.11	0.009	...	...	...	...	0.07 ± 0.18	0.001	10.2 ± 0.23	0.096
NGC 3786	0.56 ± 0.06	0.031	...	...	0.51 ± 0.02	0.031	1.49 ± 0.02	0.087	1.10 ± 0.02	0.042	0.06 ± 0.03	0.024	1.31 ± 0.19	0.066	0.04 ± 0.01	0.020	1.33 ± 0.06	0.076	1.70 ± 0.05	0.096
NGC 2622	0.62 ± 0.05	0.069	0.11 ± 0.04	0.009	0.44 ± 0.02	0.031	0.50 ± 0.02	0.031	0.91 ± 0.03	0.025	0.40 ± 0.04	0.012	0.86 ± 0.06	0.036	0.23 ± 0.05	0.009	0.59 ± 0.05	0.036	2.56 ± 0.08	0.165
NGC 5728	0.95 ± 0.10	0.061	0.42 ± 0.09	0.035	2.84 ± 0.10	0.197	2.26 ± 0.06	0.084	7.69 ± 0.06	0.162	3.85 ± 0.08	0.081	13.7 ± 0.09	0.244	...	...	6.29 ± 0.12	0.094	9.87 ± 0.17	0.145
NGC 7682	1.34 ± 0.05	0.073	...	...	0.86 ± 0.02	0.029	5.10 ± 0.02	0.164	3.79 ± 0.04	0.109	4.60 ± 0.05	0.093	4.42 ± 0.04	0.077	...	...	6.03 ± 0.09	0.102	12.2 ± 0.11	0.203

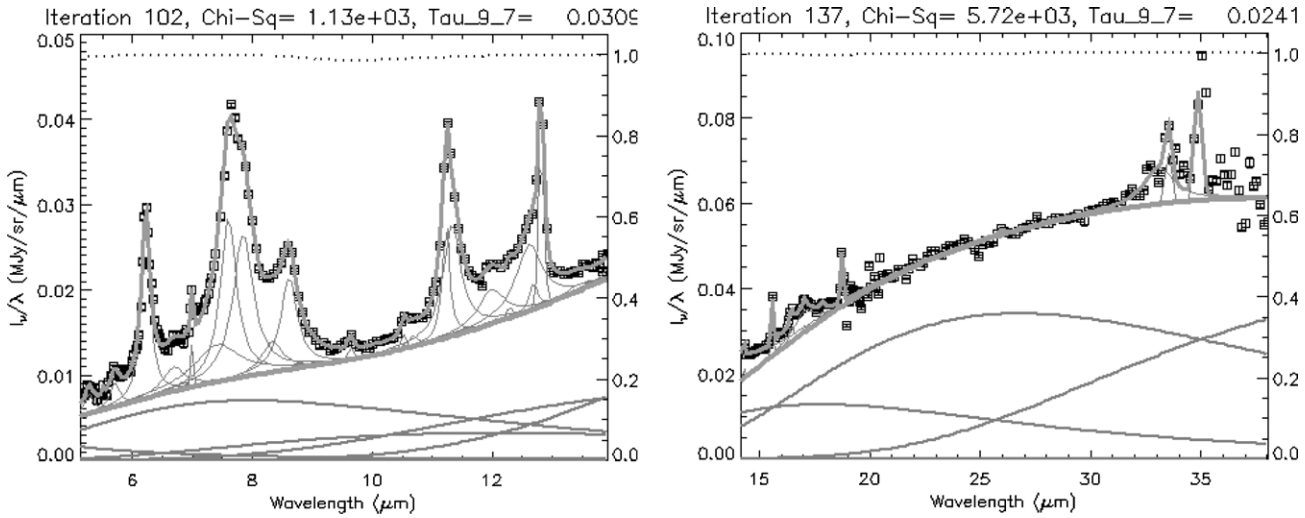

Figure 3. Detailed decomposition of Mrk 334 from 5 to 37 μm using the PAHFIT code. Solid black lines represent thermal dust continuum components. Measurements are represented by squares, and uncertainties are plotted as vertical error bars, which are smaller than the symbol size. The dotted black line indicates mixed extinction components. Continuous lines (gray) represent the best-fit model with individual PAH features and emission lines, respectively.

have a continuum shape increasing for longer wavelengths, in agreement with results found by Weedman et al. (2005), Buchanan et al. (2006), Deo et al. (2009), Burtscher et al. (2009), Wu et al. (2009), and Baum et al. (2010). This continuum range can be fitted with a warm blackbody distribution of $T \sim$ 150–300 K. Interestingly, a similar trend in the continuum of AGNs is also observed in the near-infrared region (Riffel et al. 2006, 2009).

We compare the spectroscopic properties of the 15 new objects with those of the Buchanan et al. (2006) groups. We found that the spectra of the Sy 2 galaxies, NGC 3786, NGC 5728, NGC 7682, Mrk 471, Mrk 609, Mrk 622, Mrk 883, Mrk 1066, Mrk 883, and the Sy 1 Mrk 334 and NGC 4748, have the same characteristics as their group 1 (strong PAH emission and red continuum, see Figure 2). On the other hand, the Sy 2, NGC 1275, NGC 2622, Mrk 3, and Sy 1 Mrk 478 can be classified as group 3 (power-law continuum and weak PAH features), while only the Sy 1 Mrk 279 galaxy shows a broken continuum and silicate emission at 9.8 μm (group 2). In summary, for our and Buchanan et al. (2006) samples the mid-IR spectra for most of Sy 2 galaxies have the same spectroscopic characteristics as those of group 1 ($>$ 50%).

3.2. PAH and Emission Line Frequency

Figure 4 shows a histogram of the most common emission features present in each type of activity (note that we have used the 186 galaxies' spectra). It is clear from this figure that the PAH features are present in almost all the Sy 1, Sy 2 and SB galaxies, as well as the H_2 molecules at 9.6 μm and 17 μm. In addition, the most frequent ionic lines are [Si II] 34.8 μm, [Ar II] 6.9 μm, [S III] 18.7 and 33.4 μm, [S IV] 10.5 μm, [Ne III] 15.53 μm, and [Ne V] 14.3 μm.

All studied SB galaxies show PAH bands and the following forbidden emission lines: [Si II]34.8 μm, [Ar II]6.9 μm, [S III]18.7, and 33.4 μm. In addition, nearly 80% show molecular H_2 lines. Similarly, $\geqslant$80% of the Sy 2 show PAH features, and the same ionic lines detected in SB galaxies. However, we have found that PAH lines in Sy 1 galaxies behave differently from the other types of nuclear activity. The PAH bands at 7.7 μm, 11.3 μm, and 12.7 μm are present in 80% of the galaxies, but only 50% of them show the PAH lines at 6.2 μm and 8.6 μm. Nevertheless, the high ionization lines, such as [Ne V]14.3 μm and [O IV]25.8 μm, are more common in Sy 1.

3.3. Diagnostic Diagram of PAH Bands: Grain Sizes and Ionization Fraction

Numerical studies of the vibrational energy distribution of PAH molecules show that the relative strengths of the 3.3 μm, 6.2 μm, 7.7 μm, 8.6 μm, and 11.3 μm PAH features depend on the grain size and on the charging conditions (Draine & Li 2001). Small PAHs radiate strongly at 6.2 μm and 7.7 μm, while large PAHs emit mostly at longer wavelengths (Schutte et al. 1993; Draine & Li 2007; Tielens 2008). Another important conclusion of Draine & Li (2001) is that neutral PAHs have higher values of the 11.3 μm/7.7 μm ratio, while ionized PAHs have lower ratios. On the other hand, the 6.2 μm/7.7 μm ratio decreases with the increasing number of carbon atoms of the PAH molecules; Figure 16 from Draine & Li (2001) shows how the relative strengths of these emission vary depending on the size and charge state of PAH molecules. O'Dowd et al. (2009) used this diagram to analyze these PAH ratios for a sample formed by galaxies dominated by star formation, galaxies with significant stellar and AGN component, and AGN-dominated galaxies. They found a weak trend in the direction of constant ionization fraction with changing grain size. In addition, they suggest that the presence of an AGN component is correlated with the reduction in the 7.7 μm/11.3 μm ratio indicating that smaller PAH grains (number of carbon atoms $<$180) are destroyed in AGNs.

We present in Figure 5 the theoretical intensity ratios, for neutral and ionized PAHs (6.2 μm/7.7 μm $\times$ 11.3 μm/7.7 μm), from Draine & Li (2001). The authors calculated these quantities assuming grains illuminated either by the Mathis et al. (1983) spectrum or by a blackbody with $T = 3 \times 10^4$ K varying the number of carbon atoms in each molecule. We overplot in this diagram the observed PAH emission line ratios of our sample. Clearly, the observed ratios are located between neutral and ionized PAH theoretical lines, in agreement with previous studies (Draine & Li 2001; O'Dowd et al. 2009).

The above results suggest that the observed PAH bands in both AGNs and low-ionization objects (SBs and LINERs), are formed by an appropriate mixture of PAH molecules with

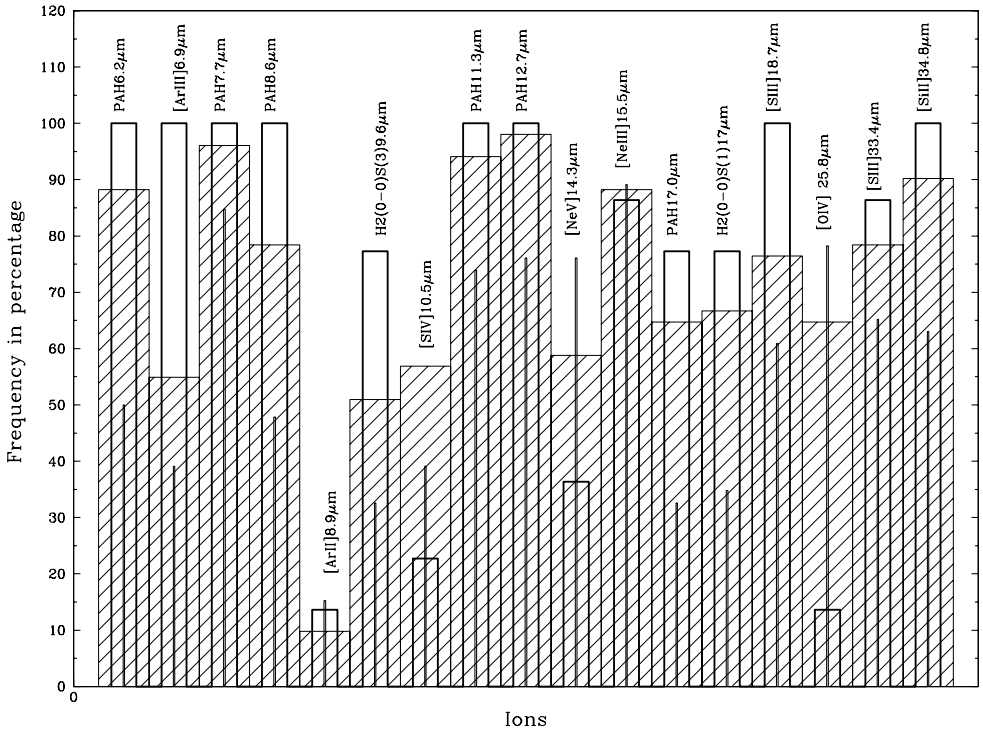

Figure 4. Frequency histogram of most common mid-IR emission lines (in percentage). SB, Sy 2, and Sy 1 are represented by empty and shaded bars, and solid lines, respectively.

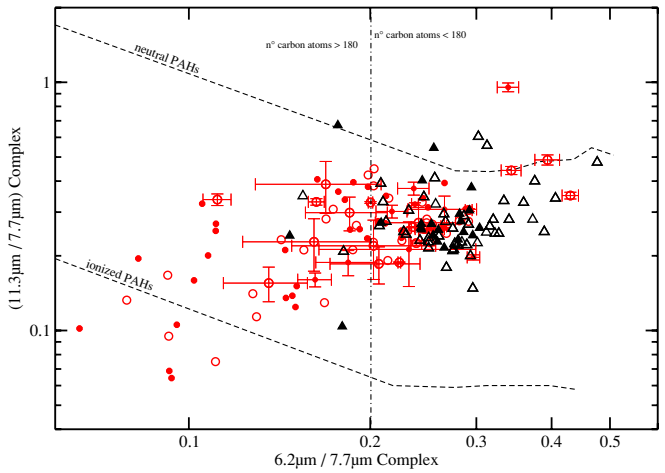

Figure 5. Diagnostic diagram of 6.2 μm/7.7 μm × 11.3 μm/7.7 μm PAH ratios. The long dashed line represents theoretical intensities of neutral to ionized PAHs (Draine & Li 2001). The dash-dotted line shows the position of molecules formed by 180 carbon atoms. Empty triangles are H II and LINER objects taken from Smith et al. (2007) and Gordon et al. (2008), full triangles are SBs taken from Brandl et al. (2006), and full and empty circles are Sy 1 and Sy 2 of our and Gallimore et al. (2010) sample. Error bars are shown only for the 15 new AGNs; similar errors were found for the remaining objects.

(A color version of this figure is available in the online journal.)

different sizes and adequate neutral to ionized fraction. High-ionization objects (AGNs) present a tendency for molecules with >180 carbon atoms (6.2 μm/7.7 μm < 0.2); on the other hand, most of low-ionization objects are biased toward molecules with less than 180 carbon atoms. The latter are typically located in the region 0.2 < 6.2 μm/7.7 μm < 0.4 (Figure 5). Furthermore, Seyfert galaxies appear to be located near to the region populated by ionized PAH molecules, while the majority of SB, H II, and, LINER are near to the line representing the neutral PAHs. Moreover, these results are consistent with a picture that AGNs have higher ionization fraction and larger PAH molecules than SB galaxies.

Another way to assess the ionization fraction of the PAH molecules is using the following diagnostic diagram: 6.2 μm/11.3 μm × 7.7 μm/11.3 μm. Such diagram was used by Galliano (2006), Galliano et al. (2008), and O'Dowd et al. (2009); they demonstrate that there is a good correlation between both ratios. However, we would like to emphasize the fact that both samples were mostly composed by SB galaxies. In addition, these ratios are controlled by the fraction of ionized to neutral PAHs (Allamandola et al. 1999).

In Figure 6 (top), we show this diagram for our sample. Clearly, if we only consider the SB galaxies, our results are consistent with the correlation described above. By including the AGNs (Sy 1 and Sy 2), an unexpected large dispersion is observed for both types of activities. Alternatively, we also test the diagram 6.2 μm/8.6 μm × 7.7 μm/8.6 μm involving ionized (7.7 μm and 6.2 μm) and neutral (8.6 μm) PAH molecules. This diagram is shown in Figure 6 (bottom), where a similar dispersion is observed. Interestingly, in both diagnostic diagrams the ratios in the vertical axes tend to separate the AGNs (Sy 1 and Sy 2) from SB galaxies. This is even clearer in the diagram involving the 7.7 μm/8.6 μm ratio, leading us to the conclusion that 7.7 μm/8.6 μm $\geqslant$ 6 for AGNs (dotted line) and smaller for low-ionization objects.

Synthetic spectra in the 6.2 μm–9.0 μm region, for large symmetric PAHs cations, anions, and neutral, have been computed by Bauschlicher et al. (2008). The trends in the band position and intensity are a function of the molecule size, charge, and geometry. Large PAH cations and anions (>110 carbon atoms) produce prominent bands at 7.7 μm and 8.5 μm, and the intensity ratio 7.7 μm/8.6 μm increases with the PAH sizes. Thus, we interpret the separation in activity types (SB, Sy 1, and Sy 2), along the vertical axis in both diagrams of Figure 6, as due to the fact that in average the emitting PAH molecules in Seyferts

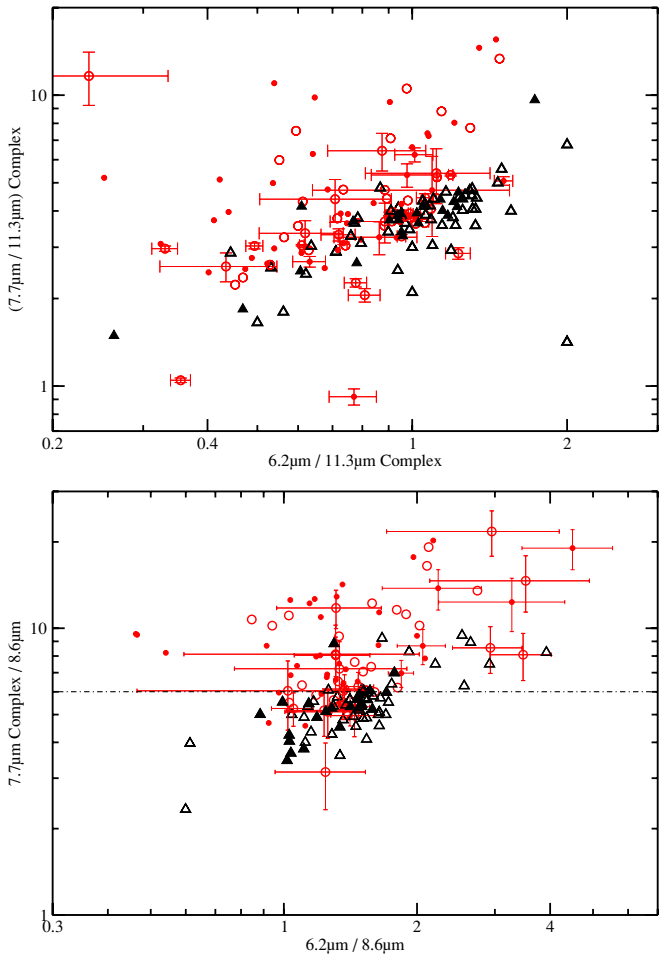

Figure 6. Diagnostic diagram of the relative strengths of the neutral (8.6 μm and 11.3 μm) compared to the ionized (6.2 μm and 7.7 μm) PAH bands. In the top, 6.2 μm/11.3 μm × 7.7 μm/11.3 μm PAHs are shown. Empty triangles are H II and LINER objects taken from Smith et al. (2007) and Gordon et al. (2008), full triangles are SBs taken from Brandl et al. (2006), and full and empty circles are Sy 1 and Sy 2 of our and Gallimore et al. (2010) sample. Error bars are shown only for the 15 new AGNs; similar errors were found for the remaining objects. The dotted line separates high- and low-ionization objects.

(A color version of this figure is available in the online journal.)

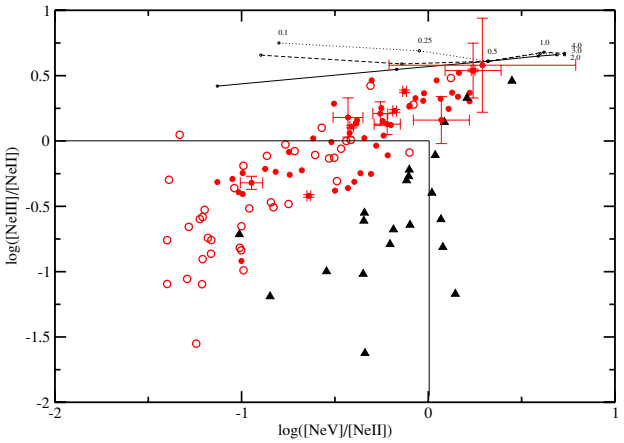

Figure 7. Diagnostic diagram of [Ne V]14.3 μm/[Ne II]12.8 μm × [Ne III]15.5 μm/[Ne II]12.8 μm ratios. The direction of increasing ionization parameter for dusty NLR models with the total pressure of $P_{\rm tot}/k \simeq 10^6$ (dotted curve), $\simeq 10^7$ (dashed curve), and $\simeq 10^8$ (solid curve). Full triangles are SBs taken from Brandl et al. (2006), and full and empty circles are Sy 1 and Sy 2 of our and Gallimore et al. (2010) sample. Error bars are shown only for the 15 new AGNs; similar errors were found for the remaining objects.

(A color version of this figure is available in the online journal.)

are larger than those of SBs. In addition, we suggest that the high values for the ratios 7.7 μm/8.6 μm and 7.7 μm/11.3 μm are due to the fact that almost all the molecules are ionized. In summary, we point out that both diagrams (Figures 5 and 6) clearly show that the ionization fraction and molecule size increase from SBs to AGNs. However, it is worth mentioning that no separation between Seyfert types is observed.

Although the four ratios depend on the PAH ionization fractions, ratios involving the 6.2 μm band have the same range of variation for both types of nuclear activities. This can be associated with the fact that the 6.2 μm PAH emission is due to small molecules (Bauschlicher et al. 2008), which probably are destroyed by the hard radiation field of Seyfert galaxies.

3.4. Diagnostic Diagram for Emission Line Objects

As shown in Section 3.2 (Figure 4), forbidden ionic emission lines are observed in SBs and active galaxies. In the first case, the gas is ionized by massive hot stars, while in the latter, the ionization is due to a non-thermal continuum. Moreover, the emission cloud in AGNs is located in the narrow line regions (NLRs; Osterbrock & Ferland 2006).

The mid-IR emission from the dusty NLR of AGNs has been explored by Groves et al. (2006). Their models give a direct connection between the dust emission and the line emission from the photoionized gas. These authors also show that the emission line ratios [Ne V]/[Ne II] × [Ne III]/[Ne II] can be used to separate AGNs from SBs. In addition, Thornley et al. (2000), using starburst evolutionary models, which incorporate new stellar atmosphere models for massive stars, found that [Ne III]/[Ne II] is sensitive to the hardness of the radiation field.

In Figure 7, we show the diagnostic diagram [Ne V]14.3 μm/[Ne II]12.8 μm × [Ne III]15.5 μm/[Ne II]12.8 μm for our sample. We also overplot the NLR models for different ionization and pressure parameters taken from Groves et al. (2006). Clearly, all the observations have values lower than those predicted by the models. In this diagram, AGNs are closely correlated, while the SB galaxies show large scattering.

The line [Ne V]14.3 μm has a high ionization potential of 97.1 eV and is often detected in the spectra of AGNs (e.g., Sturm et al. 2002; Weedman et al. 2005); however, it is rarely detected in SB galaxies (Brandl et al. 2006; Bernard-Salas et al. 2009). The lack of correlation for SB galaxies in this diagram, thus, may be due to a strong contamination of [Ne V] with PAH 14.19 μm emission or to the absence of the former line in the SB galaxies spectra. In addition, we call attention to the fact that the deblending of these lines is very difficult in the low-resolution *Spitzer* spectra.

It is also clear in this figure that Sy 1 galaxies have [Ne III]/[Ne II] $\geqslant 0$, while SB and Sy 2 have a ratio $\leqslant 0$ (solid line in Figure 7). This suggests that both line ratios are sensitive to the hardness of the radiation field, confirming the result of Thornley et al. (2000). The fact that Sy 2 galaxies are spread over the lower left of Figure 7 can be associated with Groves et al. (2006) predictions, which state that starburst contribution would move the points in that direction.

It is worth mentioning that there are 3 SB galaxies located in the top-right side of Figure 7 (NGC 1097, NGC 4676, and NGC 520). The former was reclassified as Sy 1 by Storchi-Bergmann et al. (1997), while the latter two are strongly interacting sources and may have these emission lines enhanced (Read & Ponman 1998). Thus we suggest that further, more

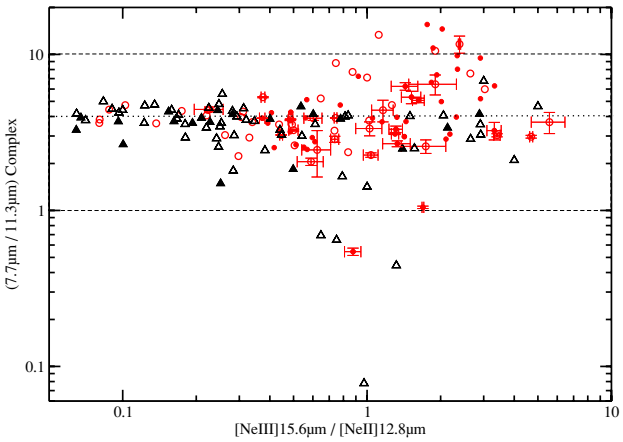

Figure 8. Diagnostic diagram between an indicator of the hardness of the radiation field and [Ne III]15.5/[Ne II]12.8 μm × 7.7 μm/11.3 μm PAH emission features. Empty triangles are H II and LINER objects taken from Smith et al. (2007) and Gordon et al. (2008), full triangles are SBs taken from Brandl et al. (2006), and full and empty circles are Sy 1 and Sy 2 of our and Gallimore et al. (2010) sample. Error bars are shown only for the 15 new AGNs; similar errors were found for the remaining objects.

(A color version of this figure is available in the online journal.)

accurate studies (i.e., with higher spectral resolution spectra) are necessary to better explain the position of the SB galaxies in the diagram.

4. BEHAVIOR OF THE IONIZATION FRACTION AND EW OF PAH MOLECULES WITH THE HARDNESS OF RADIATION FIELD

Smith et al. (2007) have studied the correlation between the intensity ratio of the strongest PAH bands 7.7 μm/11.3 μm with the hardness of the radiation field indicator, [Ne III]/[Ne II]. They have found that galaxies with H II regions or starburst optical spectra exhibit a nearly constant 7.7 μm/11.3 μm across the whole range of radiation hardness, including low-metallicity galaxies, which have [Ne III]/[Ne II] < 2. In contrast, the AGNs are located below the H II-type galaxies, and their PAH ratio falls rapidly with increasing radiation field. This result was confirmed by O'Dowd et al. (2009) through the analysis of PAH emission bands of a sample of 92 typical star-forming galaxies. They interpreted the decrease in the PAH band ratio for AGNs as due to a selective destruction of the ionized 7.7 μm PAH molecules.

The variation of 7.7 μm/11.3 μm PAH bands, observed in our sample (186 objects), with respect to the hardness of the radiation field, is shown in Figure 8. It is clear from this figure that the fraction of ionized to neutral PAH bands does not depend on the hardness of the radiation field in contrast with the previous results of Smith et al. (2007) and O'Dowd et al. (2009). We interpret this behavior as due to the fact that the strengths of both PAH bands would have the same dependence on the radiation field.

Besides, this diagram shows a tendency in the sense that SB galaxies have [Ne III]/[Ne II] < 0.4, while for Sy 1 and Sy 2, [Ne III]/[Ne II] > 0.4. In addition, Sy 1 are biased toward the location on the upper right corner. Some of the Sy 2 galaxies are located in the SB region, which suggests that these galaxies may have a circumnuclear starburst. No clear separation between Sy 1 and Sy 2 is observed for [Ne III]/[Ne II] > 0.4.

In order to test the dependence of the PAH band strength on the radiation field, we compare in Figure 9 the EW of the 7.7 μm and 11.3 μm PAH bands with [Ne III]/[Ne II] hardness indicator. It can be seen that EWs of both PAH bands are constant with

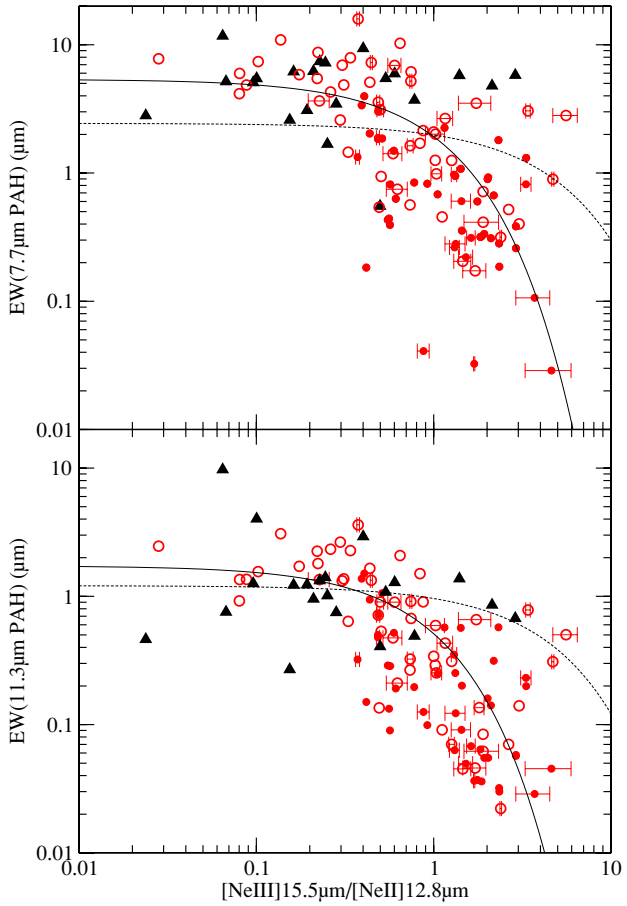

Figure 9. Diagnostic diagram between an indicator of the hardness of the radiation field and [Ne III]15.5/[Ne II]12.8 μm versus EW 7.7 μm (top) and EW 11.3 μm (bottom) PAH emission features. Full triangles are SBs taken from Brandl et al. (2006), and full and empty circles are Sy 1 and Sy 2 of our and Gallimore et al. (2010) sample. Error bars are shown only for the 15 new AGNs; similar errors were found for the remaining objects. The lines represent an exponential regression fitted for the total sample (dotted line) and for the AGN sub-sample (solid line).

(A color version of this figure is available in the online journal.)

the radiation field indicator for [Ne III]/[Ne II] ⩽ 0.8, and fall rapidly with the increasing radiation field. Galaxies, powered by star formation, have a nearly constant EW across the full range of [Ne III]/[Ne II]. While for Sy 1 the EWs of the PAH bands decrease rapidly, for the Sy 2 the EW values are distributed either in the SB or Sy 1 region. Their location in the diagram may reflect the stellar or AGNs dominant component contribution to the spectra (i.e., in some case the Sy 2 may be dominated by a non-thermal component and in other by circumnuclear massive star formation). In order to have a more quantitative analysis of Figure 9, we have computed an exponential regression taking into account all objects (AGNs+SBs, dotted line) and another for a sub-sample formed only by AGNs (solid line). For the latter we have found a correlation coefficient of ~ -0.7, while for the former we have not found any correlation (~ -0.2).

We conclude this section by arguing that both PAH molecules, either ionized (7.7 μm) or neutral (11.3 μm), may be destroyed with increasing hardness of the radiation field. We emphasize that similar results were found by Genzel et al. (1998), which compare the PAH strength with the high to low excitation line ratios for a sample of ULIRS (ultra-luminous infrared galaxies) and AGNs. In addition, Baum et al. (2010) have shown that the diagram EW PAH 6.2 μm × [Ne V] 14.3 μm/[Ne II] 12.8 μm separates AGNs from SB galaxies.

5. SUMMARY AND CONCLUSIONS

We have analyzed the emission line properties of a sample of 186 *Spitzer* galaxy spectra. One hundred seventy-one objects were taken from the literature, and we have added 15 unpublished AGN *Spitzer* spectra, taken from the public archive. The continuum properties of the 15 new spectra were also studied. Our main results can be summarized as follows.

1. The normalized mid-IR continuum spectra (at $\lambda = 23\,\mu$m), of the 15 new AGNs, steeply rise for redder wavelengths and can be fitted with a warm blackbody distribution of $T \sim$ 150–300 K.
2. The brightest PAH spectral bands (6.2, 7.7, 8.6, 11.3, and 12.7 μm) and the forbidden emission lines of [Si II] 34.8 μm, [Ar II] 6.9 μm, [S III] 18.7, and 33.4 μm were detected in all the SBs and in ∼80% of the Sy 2. Taking under consideration only the PAH bands at 7.7 μm, 11.3 μm, and 12.7 μm, we find that they are present in ∼80% of the Seyfert 1, while only half of this type of activity show the 6.2 μm and 8.6 μm PAH bands.
3. Comparison between the observed line intensity ratios of neutral and ionized PAHs (6.2 μm/7.7 μm × 11.3 μm/ 7.7 μm) with theoretical models suggests that these ratios, in Sy 1, Sy2, and SB galaxies, are produced by an appropriate mixture of PAH molecules, with different sizes and adequate neutral to ionized fraction.
4. The PAH emission lines observed in Sy 1 and Sy 2 may be due to PAH molecules with >180 carbon atoms, while for most of the low-ionization objects (SBs and LINERs), it is biased toward molecules with <180 carbon atoms. In addition, Seyfert galaxies appear to be located near to the region populated by ionized PAH molecules, while the majority of SB, H II, and LINER populate the region of neutral PAHs. These results are consistent with a picture, where Sy 1 and Sy 2 have a higher ionization fraction and larger PAH molecules than SB galaxies.
5. We have investigated the PAH line intensity ratio diagrams 6.2 μm/11.3 μm × 7.7 μm/ 11.3 μm, and 6.2 μm/ 8.6 μm × 7.7 μm/8.6 μm. The separation in activity types (SB, Sy 1, and Sy2), along the vertical axis in both diagrams, is interpreted as due to the fact that on average the emitting PAH molecules in Seyferts are larger than those of SBs, with ionization fraction and emitting molecules sizes increasing from SBs to AGNs. No separation between Seyfert types is observed.
6. A diagnostic diagram [Ne V]14.3 μm/[Ne II]12.8 μm × [Ne III]15.5 μm/[Ne II]12.8 μm shows that AGNs are correlated, while SB galaxies show large scattering. Moreover, for most of the Sy 1, [Ne III]/[Ne II] $\geqslant 0$, while for SB and Sy 2s, [Ne III]/[Ne II] $\leqslant 0$, indicating that both line ratios can be used as an indicator of radiation field hardness.
7. The ratio between the 7.7 μm and 11.3 μm PAH bands is nearly constant with the increase of [Ne III]15.5 μm/[Ne II] 12.8 μm, indicating that the fraction of ionized to neutral PAH bands does not depend on the hardness of the radiation field.
8. The EW of both PAH features (7.7 μm and 11.3 μm) shows the same dependence with the [Ne III]/[Ne II] ratio. In the case of Sy 1, they are nearly constant for [Ne III]/[Ne II] $\leqslant$ 0.8, and fall sharply with increasing radiation field. For SB galaxies, the PAH EW is constant with the increase of [Ne III]/[Ne II]. Sy 2s are distributed either in the SB or Sy 1 regions. These results suggest that the PAH molecules, emitting either ionized (7.7 μm) or neutral (11.3 μm) bands, may be destroyed with increasing hardness of the radiation field.

We thank an anonymous referee for useful comments, as well as Charles Bonatto, Daniel Ruschel-Dutra, and Rogemar André Riffel for useful discussions. This research has made use of the NASA/IPAC Extragalactic Database (NED) which is operated by the Jet Propulsion Laboratory, California Institute of Technology, under contract with the National Aeronautics and Space Administration. This work is based on observations made with the *Spitzer Space Telescope*, which is operated by the Jet Propulsion Laboratory, California Institute of Technology, under a contract with NASA.

REFERENCES

Allamandola, L. J., Hudgins, D. M., & Sandford, S. A. 1999, ApJ, 511, L155
Baum, S. A., et al. 2010, ApJ, 710, 289
Bauschlicher, C. W., Jr., Peeters, E., & Allamandola, L. J. 2008, ApJ, 678, 316
Bernard-Salas, J., et al. 2009, ApJS, 184, 230
Brandl, B. R., et al. 2006, ApJ, 653, 1129
Buchanan, C. L., Gallimore, J. F., O'Dea, C. P., Baum, S. A., Axon, D. J., Robinson, A., Elitzur, M., & Elvis, M. 2006, AJ, 132, 401
Burtscher, L., Jaffe, W., Raban, D., Meisenheimer, K., Tristram, K. R. W., & Röttgering, H. 2009, ApJ, 705, L53
Deo, R. P., Richards, G. T., Crenshaw, D. M., & Kraemer, S. B. 2009, ApJ, 705, 14
Draine, B. T., & Lee, H. M. 1984, ApJ, 285, 89
Draine, B. T., & Li, A. 2001, ApJ, 551, 807
Draine, B. T., & Li, A. 2007, ApJ, 657, 810
Galliano, F. 2006, arXiv:astro-ph/0610852
Galliano, F., Madden, S. C., Tielens, A. G. G. M., Peeters, E., & Jones, A. P. 2008, ApJ, 679, 310
Gallimore, J. F., et al. 2010, ApJS, 187, 172
Genzel, R., et al. 1998, ApJ, 498, 579
Gordon, K. D., Engelbracht, C. W., Rieke, G. H., Misselt, K. A., Smith, J.-D. T., & Kennicutt, R. C., Jr. 2008, ApJ, 682, 336
Groves, B., Dopita, M., & Sutherland, R. 2006, A&A, 458, 405
Houck, J. R., et al. 2004, ApJS, 154, 18
Hunt, L. K., Thuan, T. X., Izotov, Y. I., & Sauvage, M. 2010, ApJ, 712, 164
Kaneda, H., Onaka, T., Sakon, I., Kitayama, T., Okada, Y., & Suzuki, T. 2008, ApJ, 684, 270
Mathis, J. S., Mezger, P. G., & Panagia, N. 1983, A&A, 128, 212
O'Dowd, M. J., et al. 2009, ApJ, 705, 885
Osterbrock Donald, E., Gary, J., & Ferland, 2006, Astrophysics of Gaseous Nebulae and Active Galactic Nuclei (2nd ed.; Sausalito, CA: Univ. Science Books)
Pogge, R. W., & Owen, J. M. 1993, OSU Internal Report 93-01
Puget, J. L., & Leger, A. 1989, ARA&A, 27, 161
Read, A. M., & Ponman, T. J. 1998, MNRAS, 297, 143
Riffel, R., Pastoriza, M. G., Rodríguez-Ardila, A., & Bonatto, C. 2009, MNRAS, 400, 273
Riffel, R., Rodríguez-Ardila, A., & Pastoriza, M. G. 2006, A&A, 457, 61
Roche, P. F., Aitken, D. K., Smith, C. H., & Ward, M. J. 1991, MNRAS, 248, 606
Schutte, W. A., Tielens, A. G. G. M., & Allamandola, L. J. 1993, ApJ, 415, 397
Smith, J. D. T., et al. 2007, ApJ, 656, 770
Storchi-Bergmann, T., Eracleous, M., Ruiz, M. T., Livio, M., Wilson, A. S., & Filippenko, A. V. 1997, ApJ, 489, 87
Sturm, E., Lutz, D., Tran, D., Feuchtgruber, H., Genzel, R., Kunze, D., Moorwood, A. F. M., & Thornley, M. D. 2000, A&A, 358, 481
Sturm, E., Lutz, D., Verma, A., Netzer, H., Sternberg, A., Moorwood, A. F. M., Oliva, E., & Genzel, R. 2002, A&A, 393, 821
Thornley, M. D., Schreiber, N. M. F., Lutz, D., Genzel, R., Spoon, H. W. W., Kunze, D., & Sternberg, A. 2000, ApJ, 539, 641
Tielens, A. G. G. M. 2008, ARA&A, 46, 289
Voit, G. M. 1992a, ApJ, 399, 495
Voit, G. M. 1992b, MNRAS, 258, 841
Weedman, D. W., et al. 2005, ApJ, 633, 706
Wu, Y., Charmandaris, V., Huang, J., Spinoglio, L., & Tommasin, S. 2009, ApJ, 701, 658